



# Ion transport, dielectric, and electrochemical properties of sodium ion-conducting polymer nanocomposite: application in EDLC

Ankit Kumar<sup>1</sup> · Mohit Madaan<sup>1</sup> · Anil Arya<sup>1</sup> · Shweta Tanwar<sup>1</sup> · A. L. Sharma<sup>1</sup>

Received: 27 January 2020 / Accepted: 19 May 2020 / Published online: 28 May 2020  
© Springer Science+Business Media, LLC, part of Springer Nature 2020

## Abstract

The present paper reports the investigation of structural, electrical, dielectric, and transport properties of the polyethylene oxide (PEO)-based polymer nanocomposite (PNC), with sodium hexafluorophosphate ( $\text{NaPF}_6$ ) salt and barium titanate ( $\text{BaTiO}_3$ ) as nanofillers. The PNC has been prepared via standard solution casting technique. The structural investigation has been investigated by X-ray diffraction and evidence the enhancement in amorphous content. The morphology has been examined by Field emission scanning electron microscopy technique and confirms the composite formation. The presence of polymer–ion and ion–ion interaction has been confirmed by the Fourier transform infrared spectra (FTIR) and evidences the PNC formation. The impedance spectroscopy has been performed to evaluate the ionic conductivity in the temperature range 40–100 °C. The increase of conductivity is obtained with the addition of nanofiller and temperature-dependent conductivity follows Arrhenius behavior. The PNC film having the highest conductivity exhibits low activation energy and indicates the fast ion migration. The ion transference number is close to unity and the voltage stability window is within the desirable limit. The complex permittivity and complex conductivity have been obtained and the plot has been fitted in the whole frequency window. The fitted plot is in perfect agreement with experimental data. The PNC having the highest conductivity has high dielectric strength and low relaxation time. It confirms the nanofiller role in enhancing ion migration. The ion transport parameters ( $n$ ,  $\mu$ ,  $D$ ) are also in correlation with impedance and dielectric analysis. The optimized PNC films have been used to prepare the Electric double-layer capacitors (EDLC) and it demonstrates the improved performance which may be attributed to the effective role played by nanofiller in boosting ion dynamics.

## 1 Introduction

Owing to the increasing demand for energy and depletion of traditional energy sources (fossil fuel, coal, etc.) and impact on the environment, it becomes important to switch from non-renewable to renewable energy. The most important renewable sources of energy are solar energy, hydro energy, and wind energy. For storage of that energy, energy storage devices are required so that we can take energy when required. The most reliable, convenient, and efficient means to store electrical energy are the batteries and

supercapacitors [1–5]. Lithium-ion batteries have dominated the energy sector since its first launch in 1991 by SONY Corporation, owing to their high energy density. But, weak interfacial properties, safety, lack of Li abundance and high cost are major drawbacks of the Li-ion battery system that forces us to search alternatives of Li [6]. The sodium element (Na) is very fascinating and has the potential to fulfill the need for future energy needs. The key advantages of sodium are the sixth most abundant element (in the earth crust, 2.64%), low reduction potential (–2.7 V), low toxicity, softness, and low cost (seven times cheaper than lithium) [7]. Also, low power density is an important concern that needs to be eliminated. So, supercapacitor emerged as an attractive candidate due to high power density and fast charge–discharge, long cycle life, and good cyclic stability.

An ideal supercapacitor (SC) system comprises four components, anode, cathode, separator, and electrolyte. The existing SC system is using liquid electrolytes and separators. The former provides the path for ion migration, while later one physically separates the electrodes to

---

**Electronic supplementary material** The online version of this article (<https://doi.org/10.1007/s10854-020-03639-6>) contains supplementary material, which is available to authorized users.

---

✉ A. L. Sharma  
alsharma@cup.edu.in

<sup>1</sup> Department of Physics, Central University of Punjab, Bathinda 151001, Punjab, India

prevent short-circuit. The electrolyte used in existing SC is in liquid (aqueous or non-aqueous solution) state and results in important safety issues; leakage of flammable solvents, short-circuit, incompatibility with high energy batteries, limited commercial use due to geometry problems, and poor mechanical properties enabling their inability to go through the stress between anode and cathode [8]. So, an electrolyte is the active component in both charging and discharging operations and needs to be tuned for the effective operation of SC cell. The electrolyte for any application in energy storage/conversion devices must have (a) high ionic conductivity, (b) an electrochemical stability window ( $>4$  V), (c) a low melting point, (d) a high boiling point, (e) high electrochemical stability and good compatibility with electrodes [9–12].

Since the discovery of ion conduction in the polymer in 1973, tremendous efforts have been taken to develop a new polymer that acts as an electrolyte in energy storage/conversion devices [13]. The Polymer electrolyte (PE) is prepared by dissolving metal salts into the polar polymer matrix of high molecular weight and conductivity is linked by relation with a number of charge carriers, and ion mobility [ $\sigma = ne\mu$ ]. The electron-rich group in the polymer matrix acts as coordinating sites for the cation migration, and anion due to bulky size remains in the immobilized state [1, 14]. Further, the ion transport in the polymer salt matrix is enhanced by the addition of guest species, such as ionic liquid (IL), plasticizers. The incorporation of IL and plasticizer disrupts the polymer chain reorganization tendency and enhances the ion dynamics in a polymer matrix. But, the IL and plasticizer result in poor mechanical properties and is a drawback need to be eliminated before going to the application part. So, the only possibility that emerges is to eliminate this liquid phase by replacing it with solid polymer electrolyte (SPE). But, the conductivity of the SPE (complexed with metal salt) is not adequate for the application. The focus is to increase the ionic conductivity in SPE and can be achieved by the addition of nanofiller. The high surface area of nanofiller plays two important roles, (i) surface group ( $-\text{OH}$ ) helps in salt dissociation or release more free cations ( $\sigma \propto n$ ), and (ii) reduces the polymer chain reorganization tendency owing to Lewis acid–base interactions phenomena. Along with this the oxygen in a surface group of nanofiller (i.e.,  $-\text{OH}$ ) provides additional conducting sites for cation migration. The SPE prepared with addition of nanofiller is termed as PNC. So, the development of PNC is a feasible system to overcome all concerns raised in ionic liquid- and plasticizer-based polymer electrolyte. The prepared PNC characteristics such as free-standing nature and flexibility enable to develop the devices of varied shape and geometry [15–19].

The host polymer should have low glass transition temperature, electron donor group in the backbone, high

degradation temperature, and low barrier to bond relation leading to ease of segmental motion of polymer matrix. A number of host polymer have been used to find suitable one, poly(vinyl chloride) (PVC) [20], poly(vinyl alcohol) (PVA) [21], poly(acrylic acid) (PAA), poly(ethylene oxide) (PEO), poly(acrylonitrile)(PAN) [22], poly(vinylidene fluoride) (PVdF) [23]. Among them, PEO is the most suitable candidate owing to its low glass transition temperature, good compatibility with the salt, high degradation temperature, and presence of ether ( $-\text{O}-$ ) group [24–26]. The addition of salt having low lattice energy in the polymer matrix enhances the ion migration owing to the disruption of the crystalline nature of host polymer [27]. The sodium ion is chosen over Li due to the possibility of smaller cation size being trapped at coordinating sites of polymer matrix [28]. Various sodium metal salts have been investigated such as sodium fluoride( $\text{NaF}$ ), sodium iodide ( $\text{NaI}$ ), sodium bromide ( $\text{NaBr}$ ), sodium hexafluorophosphate( $\text{NaPF}_6$ ), sodium periodate ( $\text{NaIO}_4$ ), and sodium tetrafluoroborate ( $\text{NaBF}_4$ ). The  $\text{NaPF}_6$  (cation  $\text{Na}^+$  size = 1.02 Å and anion  $\text{PF}_6^-$  size = 2.54 Å) is most attractive salt and is used as salt. Previously, our group reported the various combination with  $\text{NaPF}_6$  salt and it was obtained that  $\text{NaPF}_6$  demonstrates superior electrical properties than other sodium salts [27, 29–31]. So,  $\text{NaPF}_6$  is chosen as salt. The incorporation of nanofiller in the polymer salt matrix is a fascinating approach to enhance ion migration in the PNC matrix. The key role played by Lewis acid–base interaction between polymer, salt, and nanofiller (i) helps in salt dissociation, (ii) disrupts polymer crystallization tendency, and (iii) provides conducting sites for ion migration. So, various nanofillers have been tried to achieve maximum ion transport, like  $\text{SiO}_2$ ,  $\text{TiO}_2$ ,  $\text{Al}_2\text{O}_3$ ,  $\text{BaTiO}_3$ , etc. [32, 33]. The high value of dielectric constant makes  $\text{BaTiO}_3$  an attractive candidate, as high dielectric constant is linked with better polarization. As per our knowledge, the effect of nanofiller with the PEO- $\text{NaPF}_6$  polymer matrix has not been investigated with  $\text{BaTiO}_3$  nanofiller. Herein, the present report is focused on the investigation of structural, electrical, dielectric, and electrochemical properties of polymer nanocomposites. The dielectric parameters have been simulated to explore the ion dynamics.

## 2 Experimental section

### 2.1 Material used

PEO (Mol. wt. =  $1 \times 10^6$  g mol $^{-1}$ ),  $\text{NaPF}_6$  (Mol. wt. = 167.95 g mol $^{-1}$ ), and  $\text{BaTiO}_3$  ( $<100$  nm particle size) nanofiller were purchased from Sigma-Aldrich, India and used. The solvent acetonitrile was purchased from Lobha Chemicals, India. The solution casting technique is used in

which magnetic stirrer, weighing machine, with petri dish are required.

## 2.2 Preparation method

The solution casting technique has been adopted for the preparation of SPE films. For that PEO (0.5 g) is used as host polymer which has been dissolved in 15 ml of Acetonitrile. The solution is now put on the magnetic stirrer for 12 h. Thereafter optimized salt with  $\ddot{O}/Na$  ratio of 8 is added and stirred again for 8 h. The optimum ratio of salt is obtained in the previous report from our group [30]. When the completely homogenous solution is obtained, the nanofiller  $BaTiO_3$  is added with a concentration of 3%, 5%, 7%, 10%, and 15% and stirred for 20–24 h. The nanofiller is sonicated separately before adding into the polymer salt complex. The obtained polymer solution is then cast in the petri dish and placed in a vacuum oven for 12 h. The thin films are kept in a desiccator for further characterization.

## 2.3 Characterization techniques

The microstructural information was obtained by X-ray diffraction (XRD) with  $CuK_{\alpha}$  radiation ( $\lambda = 1.54 \text{ \AA}$ ) in the Bragg's angle ( $2\theta$ ) range from 10 to  $70^\circ$ . Morphological studies are examined using the field emission scanning electron microscopy (FESEM). The investigation of interactions among various components of polymer nanocomposite is obtained using Fourier transform infrared (FTIR) spectroscopy (Model: Bruker Tensor 27, Model: NEXUS-870) recorded in absorbance mode in the wavenumber region  $400\text{--}4000 \text{ cm}^{-1}$ . Electrical properties like bulk resistance, ionic conductivity have been examined via Complex Impedance Spectroscopy (CIS 760; USA) for the frequency range 1 Hz–1 MHz and in the temperature range of  $40\text{--}100^\circ\text{C}$ . An AC signal of 10 mV is applied to the PNC sample, sandwiched between stainless steel electrodes, in the cell configuration SSIPNCISS.

The thermal activation energy ( $E_a$ ) for ionic transport was carried out from the slope of the linear fit of the Arrhenius plot between  $\log(\sigma)$  and  $1000/T$ . As  $\sigma = \sigma_0 \exp(-E_a/kT)$ , where  $\sigma_0$  is the constant pre-exponential factor,  $E_a$  is the activation energy,  $T$  is the absolute temperature, and  $k$  for the Boltzmann constant. The ion transference number ( $t_{ion}$ ) is calculated by  $i-t$  characteristics by applying a DC signal of 10 mV across cell configuration. The linear sweep voltammetry (LSV) is performed for obtaining the operating voltage window of the PNC films. Thermal stability analysis has been performed using thermogravimetric analysis (TGA-SHIMADZU-DTG-60H). Dielectric properties of SPE films in terms of complex permittivity, tangent loss, and complex conductivity have been analyzed from impedance data via established theoretical expressions to convert in dielectric

format [34]. Then using the best PNC film, EDLC cell has been fabricated to demonstrate the beauty of prepared PNC film as the electrolyte. The sample code is designated as PP, PPS, PPS3, PPS5, PPS7, PPS10, PPS15 for pure polymer, polymer salt, polymer salt with 3, 5, 7, 10, 15 wt% nanofiller, respectively.

## 3 Results and discussion

### 3.1 XRD analysis

The structural investigations of the prepared PNC film have been examined by the X-ray diffraction ( $2\theta$  from  $10^\circ$  to  $70^\circ$ ). Figure 1i shows the XRD pattern for the pure polymer, polymer salt, and polymer salt with different nanofiller contents. For clear and better analysis, the XRD pattern of pristine nanofiller is also shown (Fig. 1i(h)). Two sharp crystalline peaks located at  $19.3^\circ$  and  $23.2^\circ$  are characteristic peaks of PEO, corresponding to (120) and (112), (032) planes, respectively (Fig. 1i(a)) [35]. The addition of salt in the PEO matrix, effectively suppresses the crystalline nature of PEO, as evidenced by the decrease of both characteristics peak of PEO. The polymer chain interaction with the cation and the anion of dissociated salt alters the polymer chain ( $-O-\cdots Na^+$ ). Also, a little hump is observed corresponding to peak  $23.2^\circ$  and it evidences the significant enhancement of amorphous content.

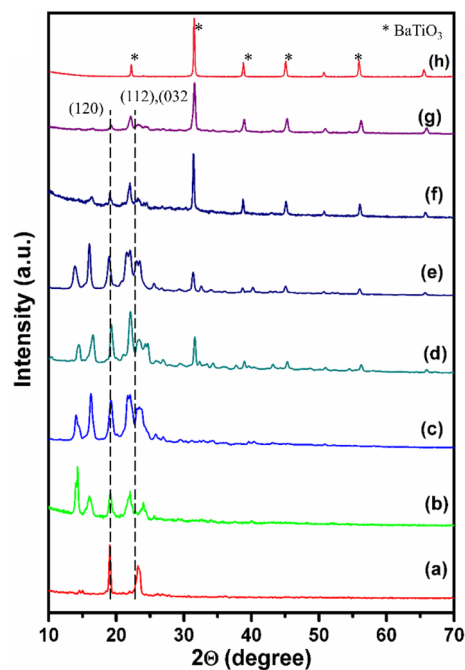


**Fig. 1** (i) XRD patterns of (a) PP, (b) PPS, (c) PPS3, (d) PPS5, (e) PPS7, (f) PPS10, (g) PPS15, and (h) Pristine  $BaTiO_3$

Further addition of nanofiller affects the crystalline nature of the polymer and lowering of peak intensity and peak broadening ( $23^\circ$ ) confirms the PNC formation and realization of amorphous content. The shift of crystalline peak to broad with the hump is the signature of the lowering of crystalline content and is beneficial for the fast ion transport. It is important to note that no peak corresponding to salt was observed and confirms the complete salt dissociation in the polymer matrix. The appearance of two peaks near  $\sim 13^\circ$ ,  $\sim 16^\circ$  are not of PEO and salt. These are associated with the formation of long-range order and may be due to the presence of ion multiplets (as  $\text{Na}_2\text{X}^+$ ,  $\text{NaX}_2^-$ ) [36, 37].

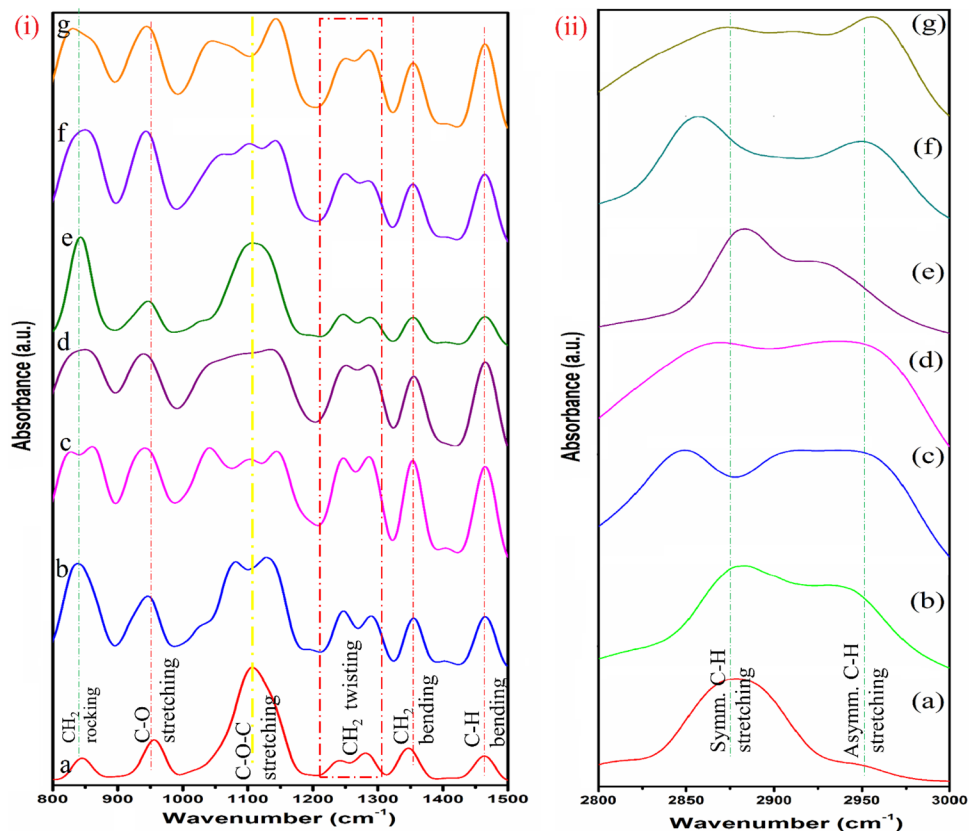
### 3.2 FTIR analysis

The FTIR spectrum of the prepared PNC film is shown in Fig. 2 and polymer–ion interaction, ion–ion interaction, and polymer–ion–nanofiller interaction have revealed. The FTIR spectrum is obtained in the absorbance mode in the wavenumber range  $400\text{--}4000\text{ cm}^{-1}$ . The FTIR spectra confirm the presence of PEO, salt, and  $\text{BaTiO}_3$  in the PNC matrix evidenced by their characteristics band. The band at  $845\text{ cm}^{-1}$  is attributed to  $\text{CH}_2$  rocking with a small contribution of C–O stretching, while band located at  $956\text{ cm}^{-1}$  is associated with C–O stretching with some  $\text{CH}_2$  asymmetry rocking (Fig. 2i(a)). The band located at  $1107\text{ cm}^{-1}$

is linked to symmetric and asymmetric C–O–C stretching in PEO. Then, the peaks at  $1241\text{ cm}^{-1}$  and  $1280\text{ cm}^{-1}$  are attributed to symmetric and asymmetric  $\text{CH}_2$  twisting of PEO. The peaks near  $1347\text{ cm}^{-1}$  and  $1463\text{ cm}^{-1}$  are assigned to  $\text{CH}_2$  bending and C–H bending of  $\text{CH}_2$ , respectively, of PEO [38]. The broadband located in the wavenumber range  $2800$  and  $3000\text{ cm}^{-1}$  is corresponding to asymmetric C–H stretching of  $\text{CH}_2$  of PEO [39].

When salt is added in the PEO matrix, then the noticeable changes are observed in the PEO spectra. The characteristic peak of PEO located at  $1107\text{ cm}^{-1}$  (symmetric and asymmetric C–O–C stretching) shows asymmetry in peak and peak broadening is evidenced (Fig. 2i(b)). The peak broadening is owing to the interaction between the cation ( $\text{Na}^+$ ) and the ether group of PEO. The broadening of the peak also indicates the enhancement of amorphous content due to the disruption of the crystalline part and facilitates the fast ion dynamics. Also, the band observed in  $2800$  and  $3000\text{ cm}^{-1}$  confirms the effective role played by salt in modifying the polymer chain interactions (Fig. 2ii(b)). Further, with the addition of nanofiller in polymer salt matrix, change in peak shape and intensity confirms the PNC formation. The characteristics band of PEO, near  $1100\text{ cm}^{-1}$  gets broadened. This indicates the cation coordination with the addition of salt, and nanofiller addition alters the shape and position of this peak which indicates

**Fig. 2** FTIR spectrum and band assignment for polymer electrolyte films (a) PP(b) PPS,(c) PPS3, (d) PPS5, (e) PPS7, (f) PPS10, and (g) PPS15 for wavenumber region, (i)  $800\text{--}1500\text{ cm}^{-1}$ , and (ii)  $2800\text{--}3000\text{ cm}^{-1}$



the nanofiller role in modifying the interaction between polymer and salt.

### 3.3 Ion–ion interaction

Further, the FTIR spectra are investigated in detail by examining the ion–ion interactions corresponding to anion vibration modes of  $\text{PF}_6^-$  in the wavenumber region from 800 to  $900\text{ cm}^{-1}$ . The reason behind the investigation centered toward deconvolution of anion mode is that cation ( $\text{Na}^+$ ) is IR inactive [40]. The anion peak shows asymmetry, which leads to the loss of degeneracy from octahedral symmetry  $O_h$  to  $C_{3v}$ . So, the free anion ( $\text{PF}_6^-$ ) and ion-pair ( $\text{Na}^+-\text{PF}_6^-$ ) contribution are evaluated by deconvolution using a Voigt Amp profile (via peak fit software). A quantitative estimation the Free ions and ion-pair contribution is calculated using Eq. 1a, 1b;

$$\text{The fraction of free anion} = \frac{\text{Area of free ion peak}}{\text{Total peak area}} \quad (1a)$$

$$\text{The fraction of ion – pair} = \frac{\text{Area of the ionpair peak}}{\text{Total peak area}} \quad (1b)$$

The peak at low wavenumber is attributed to the free ion and high wavenumber peak to the ion pair (Fig. 3). The free ion and ion-pair estimation are represented in Table 1. It may be observed that the fraction of free ions increases with the addition of nanofiller. The highest free ion area is for the PPS5 sample and the corresponding ion-pair area is minimum. The highest free ion area is associated with the highest ionic conductivity and is in correlation with the impedance study as discussed in the next section. The decrease of fraction of free ion area at high nanofiller content is due

**Table 1** The peak position and area of the deconvoluted free ion and ion pair of different samples

Sample	Free ion		Ion pair		Corr. coeff. ( $r^2$ )
	Peak position	Area	Peak position	Area	
PPS	828	52.92	843	47.07	0.9871
PPS3	822	59.63	831	40.36	0.9904
PPS5	829	68.34	844	31.35	0.9842
PPS7	830	41.50	844	58.49	0.9916
PPS10	827	53.77	843	46.22	0.9819
PPS15	823	58.20	835	41.78	0.9866

to incomplete salt dissociation and dominance of ion-pair formation. This is further confirmed by the impedance and dielectric analysis in forthcoming sections.

### 3.4 Complex impedance spectroscopy

The electrical properties were studied in this section using impedance spectroscopy. The impedance analysis of the PNC films was carried out by sandwiching the film between two stainless steel (SS) discs acting as blocking electrodes under an applied electric field. Figure 4a shows the Nyquist plot and log–log representation is used. The log–log representation advantage is reported somewhere [41]. All Nyquist plots comprise one semi-circular arc in the high-frequency region and one in the low-frequency region. The high-frequency arc provides information about the bulk properties of electrolytes such as bulk resistance and reveals that conduction is mainly due to ions. The low-frequency arc is associated with double-layer capacitance and charge-transfer resistance at the electrolyte/electrode interface. It may be noted that with the addition of salt

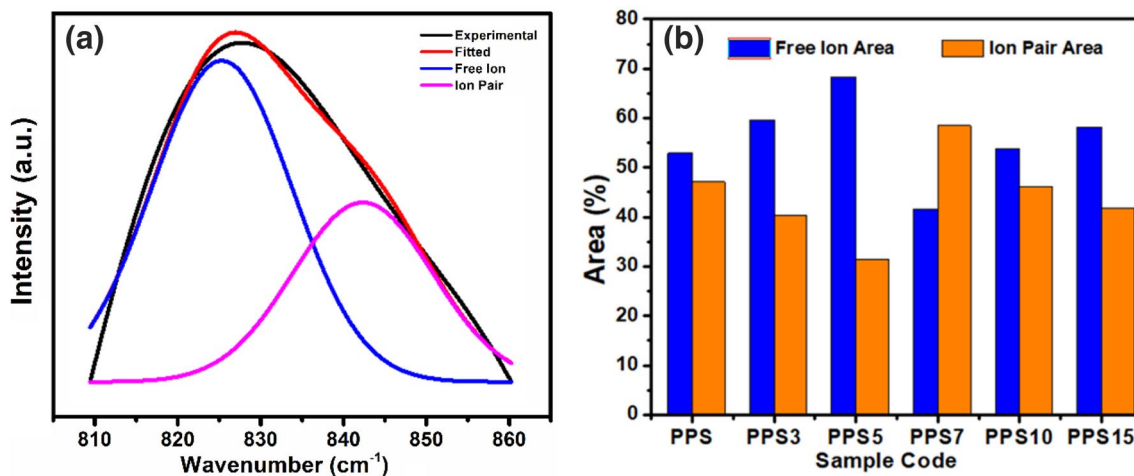


**Fig. 3** a Deconvolution of the  $\text{PF}_6^-$  vibration modes in the wavenumber region from 810 to  $860\text{ cm}^{-1}$  for PPS5, b variation of fraction of free ion and ion pair



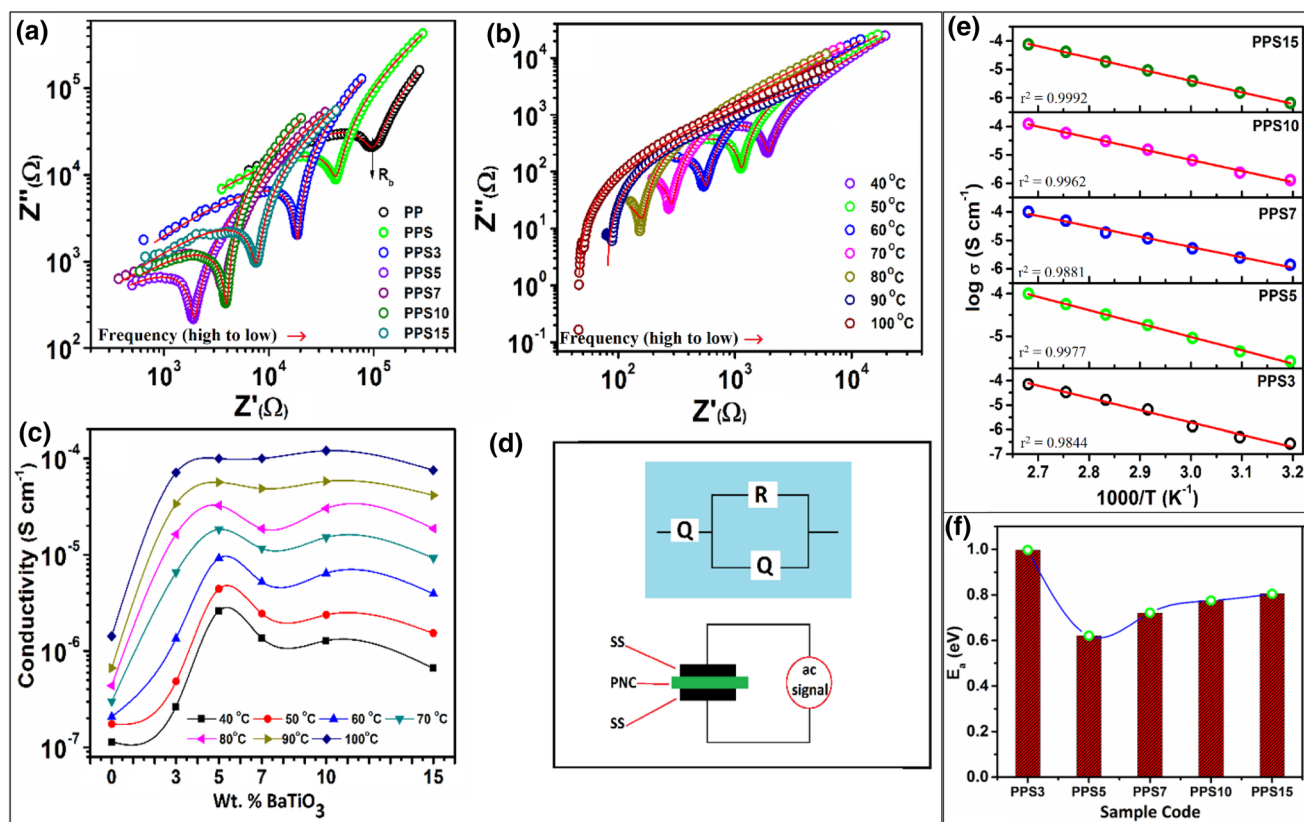


**Fig. 4** Complex impedance plot for **a** polymer electrolytes of different concentrations of nanofiller and **b** sample PPS5 with temperature variation. **c** Variation of conductivity with the concentration of BaTiO<sub>3</sub> filler for temperature variation, **d** equivalent circuit for solid

polymer electrolyte, **e** fitted Arrhenius plot, and **f** activation energy plot for polymer electrolytes dispersed with different concentrations of nanofiller BaTiO<sub>3</sub>

and nanofiller, the high-frequency arc length decreases, while low-frequency arc length decreases. The dip in low frequency corresponding to minima in the imaginary part of impedance ( $Z''$ ) indicates the bulk resistance ( $R_b$ ). The addition of salt and nanofiller shifts the dip toward low impedance value that indicates a decrease of bulk resistance [42, 43]. The lowest value is observed for the system PPS5. This confirms that nanofiller effectively enhances the ion migration and also supports salt dissociation. The optimum system is PPS5 and Fig. 4c shows the temperature dependence of the Nyquist plot. With the increase of temperature, the bulk resistance decreases as evidenced by the shift of dip toward the left side. This is attributed to the thermal activation of charge carriers and enhanced polymer flexibility. The Nyquist plot is also modeled using an electrical circuit via  $Z_{\text{Simpwin}}$  software and the fitted equivalent circuit is shown in Fig. 4d. The fitted equivalent circuit element consists of a constant phase element ( $Q$ ) in series with the parallel combination of constant phase element ( $Q$ ) and resistance ( $R$ ). The solid line in Fig. 4a, b is the fitted plot. The equivalent circuit modeling indicates excellent agreement between the theoretical data (solid

line) and experimental data points in the whole frequency range. The ionic conductivity has been obtained using the following equation for all PNC films;

$$\sigma = \frac{t}{R_b A}, \quad (2)$$

where  $t$  is sample thickness in cm,  $R_b$  is bulk resistance, and  $A$  is SS electrode area in cm<sup>2</sup>. The ionic conductivity variation for different PNC films are shown in Fig. 4c. At 40 °C, the conductivity increases with the addition of salt and is attributed to the increase of free ions in the polymer matrix and migrates via coordinating sites provided by ether group (–O–) in polymer chain. With small nanofiller loading in polymer salt matrix, an increase in conductivity is observed. This increase is due to an increase in free ions owing to improved salt dissociation. The Lewis acid–base interactions enhance the number of free ions in matrix and also lowers the polymer chain reorganization tendency. It leads to the enhancement of ionic conductivity. With the increase of nanofiller loading, ionic conductivity increases and exhibits maxima for PPS5 sample (5% nanofiller). At this particular

nanofiller content, balanced interaction between the polymer, salt, and nanofiller leads to maximum enhancement in conductivity. This may be due to three reasons, (i) complete dissociation of salt and suppression of ion-pair formation, (ii) surface group of nanofiller modifies the polymer chains arrangement and makes it flexible, and (iii) additional conducting sites provided by the surface group (–OH) of nanofiller. When nanofiller loading is increased beyond 5%, the decrease of ionic conductivity is observed. This decrease is attributed to the possibility of nanofiller aggregation and nanofiller is not effective in dissociating salts that lead to ion-pair formation. Also, at high nanofiller content, there is a probability of cation trapping and also blocks the conductive pathways for ion migration [43]. This automatically lowers the number of charge carriers in the polymer matrix and reduces the conductivity as well as ion mobility. The same trend is observed with the increase of temperature from 40 to 100 °C. With the increase of temperature enhancement in the ionic conductivity is observed. This is attributed to thermal activation of charge carriers, enhanced ion mobility, and enhanced polymer flexibility or segmental motion.

### 3.4.1 Temperature-dependent conductivity studies

The temperature-dependent ionic conductivity is further examined to evaluate the activation energy ( $E_a$ ) which is a crucial parameter that affects ion migration. The low activation energy facilitates fast ion migration. Figure 4e shows the variation of ionic conductivity ( $\log \sigma$ ) vs  $1/T$  for various PNC films. The plot is fitted with the Arrhenius Eq. 3 as given below

$$\sigma = \sigma_{0exp} \left( -\frac{E_a}{kT} \right), \quad (3)$$

where  $\sigma_0$  is the pre-exponential factor,  $E_a$  is the activation energy,  $k$  is Boltzmann constant and  $T$  is absolute temperature [44]. The  $r^2$  value is close to unity for all and indicates excellent agreement between the experimental and fitted data. The activation energy value has been plotted with a nanofiller concentration in Fig. 4f. It may be noted that the activation energy value decreases with filler concentration and is lowest for the system PPS5. The lowest activation energy value is observed for the PNC film exhibiting the highest ionic conductivity. At, high nanofiller content it again increases and is in correlation with conductivity variation [45].

### 3.5 Ion transference number and linear sweep voltammetry analysis

To support the ionic conductivity study, the measurement of ion transference number ( $t_{ion}$ ) measurement needs to be

examined. As in PNC film, both electrons and ions contribute to the total conductivity, however, the ionic contribution is a key requirement. For highly conducting PNC, a high ion transference number and negligible electron contribution is desirable. Figure 5i displays the polarization plot (current vs time) for different PNC films. All plots show the same trend, initially current is very high and is a contribution from the flow of both electrons and ions ( $I_t = I_e + I_{ion}$ ), and with the passage of time thereafter steady state is noticed. The high current is due to the dominance of polarization by an applied field that results in ion accumulation on the interface. After the passage of time, the sufficient polarization build-up and further ion migration blocked that lower the current [46–48]. The ion transference number has been calculated and is shown in Table 2. The optimized system shows almost unity ion transference number and confirms the ion conduction in PNC with a negligible electronic contribution [27, 49].

The voltage stability of the PNC film needs to be examined before using it as electrolyte cu separator for device application. The voltage stability window has been examined by the LSV technique. Figure 5ii shows the LSV plot for different PNC films in the voltage window of  $-3$  V to  $+3$  V. In the LSV plot, the sudden rise in current is taken as breakdown voltage and depicts the safe limit of electrolyte before breakdown. The voltage stability window has been obtained and is summarized in Table 2. It may be noted that the nanofiller-based PNC shows improved voltage stability window than polymer salt film (Fig. 5ii). The optimized system having the highest ionic conductivity (PPS5) possess a voltage stability window of about  $\sim 4.1$  V.

### 3.6 TGA analysis

For safe cell operation, the thermal stability of electrolytes is a crucial parameter. The thermal stability of prepared PNC film has been examined by Thermo-gravimetric analysis (TGA). TGA is performed in the temperature range of 30–580 °C (Fig. 6). The first region shows the drop of  $\sim 2\%$  up to 100 °C and is due to the evaporation of moisture in the PNC during sample loading. With an increase of temperature, a constant region is obtained up to 150 °C, followed by rapid loss after 200 °C ( $\sim 8\%$ ). This weight loss may be due to the breaking of weak polymer bonds leading to degradation. At high temperature (region-iii), rapid weight loss is observed for all samples (see table as shown in inset of Fig. 6). It is important to note that PPS system shows a rapid loss, while nanofiller-based PNC shows step loss. The region-iv shows complete loss and degradation is evidenced [27, 50]. So, it may be concluded that the prepared PNC film shows good thermal stability up to 200 °C with negligible loss.

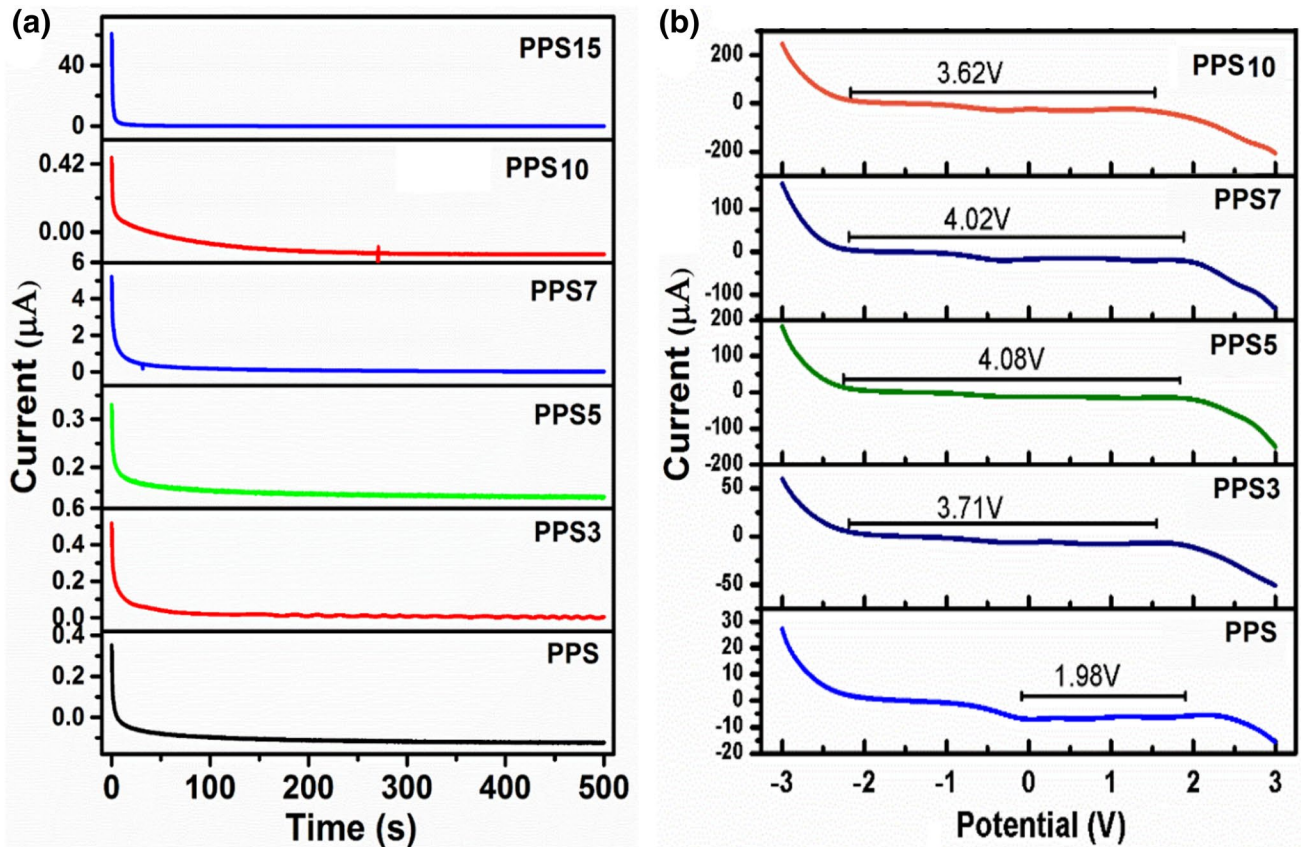


**Fig. 5** **a** Polarization current vs time curve, and **b** linear sweep voltammograms (LSVs) for different PNC films

**Table 2** Conductivity, transport number, electrochemical stability window, and activation energy value for prepared PNC films

Sample code	Ionic conductivity ( $S\text{ cm}^{-1}$ ) at $40\text{ }^{\circ}\text{C}$	$t_{\text{ion}}$	LSV (V)	$E_a$ (eV)
PPS	$1.14 \times 10^{-7}$	–	1.98	–
PPS3	$2.66 \times 10^{-7}$	0.99	3.71	0.99
PPS5	$2.61 \times 10^{-6}$	0.98	4.08	0.62
PPS7	$1.36 \times 10^{-6}$	0.99	4.02	0.72
PPS10	$1.28 \times 10^{-6}$	0.91	3.62	0.78
PPS15	$6.62 \times 10^{-7}$	0.99	2.82	0.81

### 3.7 Complex permittivity analysis

To get insights into ion dynamics in the PNC films, dielectric properties need to be explored. In the dielectric analysis, the important parameter that influences the ionic conductivity is the dielectric constant and relaxation time. The high value of the dielectric constant and low value of relaxation time suggest high ionic conductivity in polymer nanocomposites, and the impedance spectroscopy data can be represented in the different representations as complex permittivity, complex conductivity, and loss tangent. The

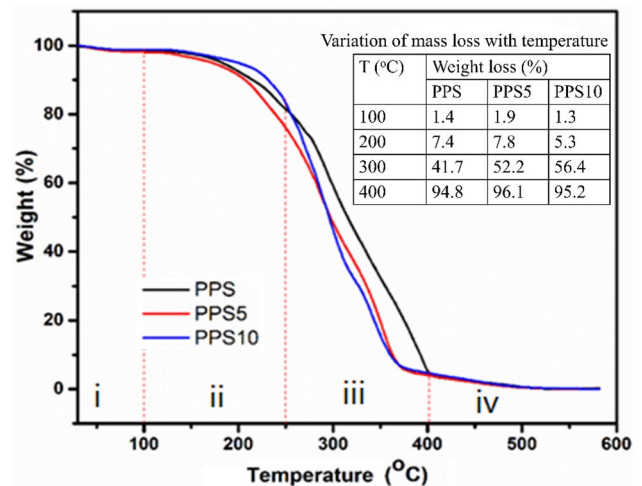


**Fig. 6** TGA curve for samples PPS, PPS5, and PPS10 for different temperature regions

complex permittivity comprises of two parts and denoted as  $\epsilon^* = \epsilon' - i\epsilon''$ , where  $\epsilon'$  is a real part of permittivity (dielectric constant) and  $\epsilon''$  is an imaginary part of permittivity (dielectric loss). The real part ( $\epsilon'$ ) tells about polarization



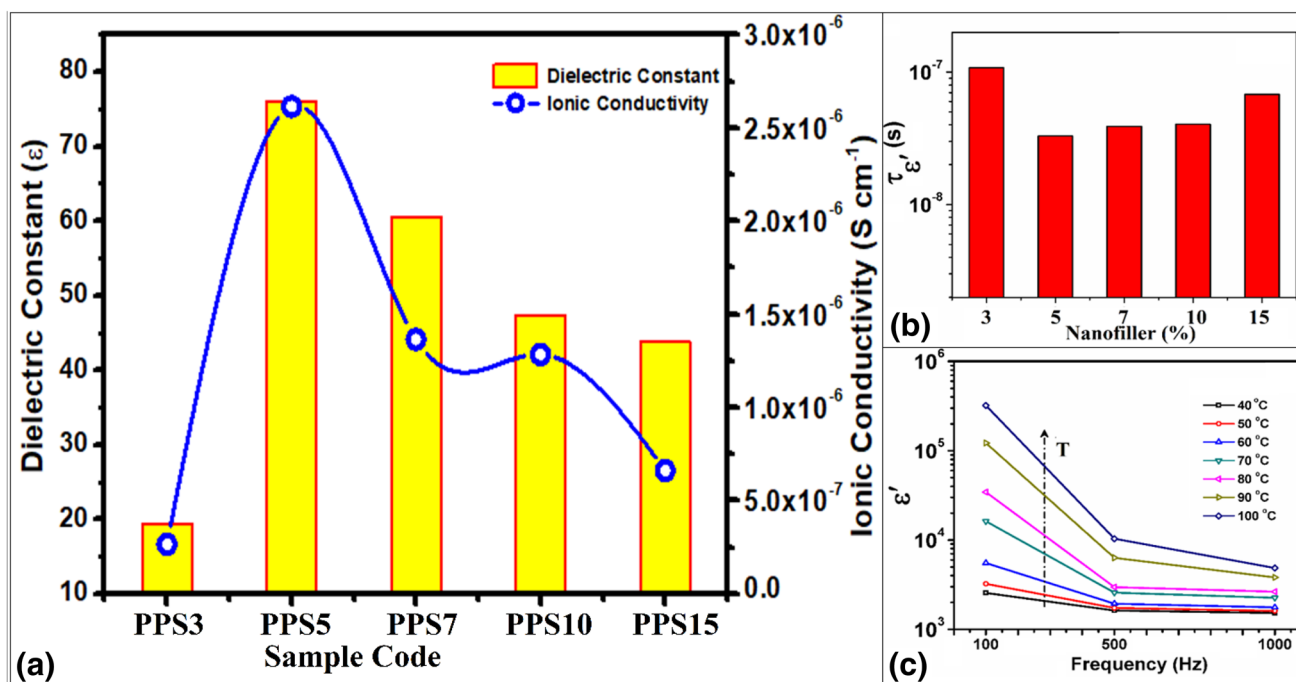
ability of charge carriers, while imaginary part ( $\epsilon''$ ) represents the energy needed to align the dipoles [34, 51].

Figure S1a shows the variation of dielectric constant ( $\epsilon'$ ) with different nanofiller contents. All PNC films follow the same trend. The high value in the low-frequency region and decreases with the increase of frequency. The high value is due to the dominance of the space charge effect. Here, in this region, dipoles follow the applied electric field and ion accumulation at the electrode/electrolyte interface leads to a build up of polarization or high dielectric constant value. With the increase of frequency, the dielectric constant value decreases and is attributed to the ion ability to follow the applied field direction. Now, the rapid periodic reversal of the field prevents the ion accumulation and a decrease of dielectric constant is observed [52–57]. The high value of the dielectric constant is observed for the PNC film having the highest ionic conductivity value and lowest activation energy (PPS5). It evidences the increase of the ions contributing to electric double-layer capacitance. Also, the high value of dielectric constant suggests the high conductivity [58, 59].

Figure S1b shows the temperature variation of the real part of the complex permittivity against frequency. It may be noted that the dielectric constant increases with the temperature and suggests the enhancement in the number of charge carriers. This enhancement is due to the thermal activation of charge carriers and improved ion

polarization. This also supports the impedance study which shows enhancement of ionic conductivity with temperature.

Figure S1c shows the variation of the imaginary part of complex permittivity or dielectric loss ( $\epsilon''$ ). This also follows the same trend as of real part of the complex permittivity. In low frequency, the high loss is due to sufficient time taken by dipole for orientation w.r.t field [60, 61]. In the high-frequency window, the film follows a different mechanism. Now, due to the periodic reversal of the field, a three-step process occurs before the reversal of direction. Initially, with a change of field direction de-acceleration of the ions occurs, followed by ion halt for a negligible time. Finally, the ion gets accelerated in the reverse direction. This mechanism results in the generation of internal heat and is termed as dielectric loss [27, 34, 62–64]. Both the real part and imaginary part of the complex permittivity plot are fitted with corresponding equations reported somewhere [34]. It may be observed that the bot experimental and fitted plot are in good agreement with each other. The variation of dielectric constant against ionic conductivity is shown in Fig. 7a, and it confirms the correlation between both. From the fitted plot, relaxation time has been plotted in Fig. 7b. It may be noted that the PPS5 having the highest ionic conductivity shows the lowest relaxation time. The lowest relaxation time facilitates the fast ion migration via conducting sites in the polymer matrix [64–67]. This is also a correlation with the



**Fig. 7** a Plot of dielectric constant vs ionic conductivity, b variation of relaxation time, and c variation of dielectric constant for PPS5 at different frequencies and temperatures

activation energy. So, PPS5 exhibits maximum conductivity and lowest activation energy as well as relaxation time.

Further, the dielectric constant value is examined with temperature and frequency for the optimum system. Figure 7c shows the plot of dielectric constant with temperature. The increase of dielectric constant is observed with temperature and is in correlation with impedance study and activation energy measurement. The high value of the dielectric constant is due to improved salt dissociation (increased free charge carriers;  $n \propto T$ ) attributed to thermal activation of charge carriers [68, 69]. In the case of polymer electrolytes, the number of charge carriers ( $n$ ) is related to dissociation energy ( $U$ ) and the dielectric constant ( $\epsilon$ ) [ $n = n_{0exp}(-U/\epsilon kT)$ ].

### 3.8 Tangent loss analysis

The loss tangent plot is examined to evaluate the relaxation time for prepared PNC film. The low relaxation time indicates the faster ion migration from one coordinating

site to another and hence high ionic conductivity. The loss tangent ( $\tan \delta = \epsilon''/\epsilon'$ ) vs. frequency plot is shown in Fig. 8. All the PNC film follows the same trend. Initially, loss increases with the increase of frequency and then at a particular frequency (here  $\omega\tau = 1$ ) loss is maximum. Then again decrease with frequency is observed. The low-frequency loss is attributed to the dominance of resistive element over capacitive. The relaxation peak indicates that ion conduction is via polymer segmental motion. At this particular frequency, the maximum transfer of energy occurs on the application of the field. The decrease in the high-frequency window is due to the dominance of the capacitive element [70, 71]. It is important to note that the relaxation peak shifts toward the high-frequency region with the addition of nanofiller in the polymer salt matrix. The lowest relaxation time for the PPS5 system indicates highest ionic conductivity [72, 73]. The loss tangent plot is fitted with the corresponding equation to evaluate the relaxation time proposed by our previous report [34]. Two relaxation times are evaluated,  $\tau_{\tan\delta}$  and  $\tau_m$  and both

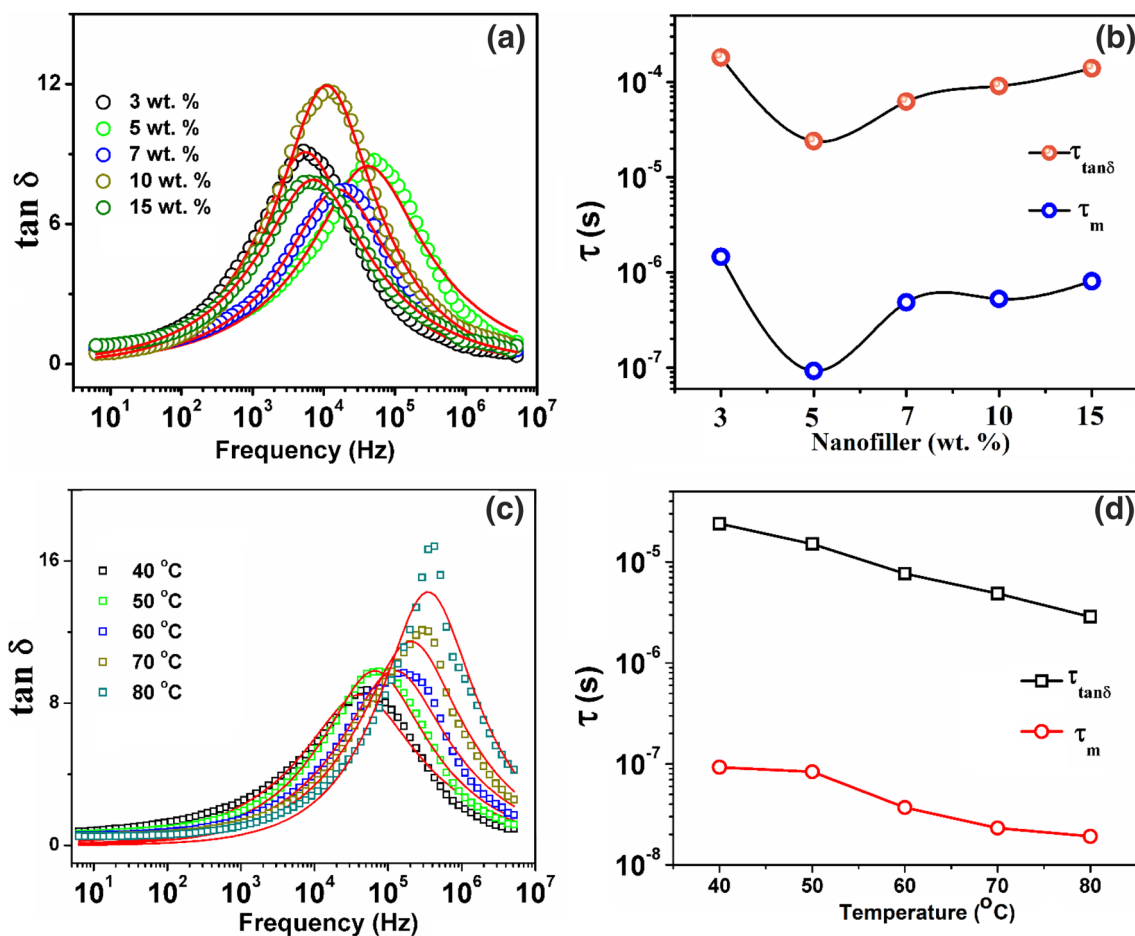


**Fig. 8** a Frequency dependence of loss tangent ( $\tan \delta$ ) for different nanofiller contents, b dependence of relaxation time on filler concentration, c temperature-dependent loss tangent plot, and d variation of relaxation time with temperature for PPS5

show minima for PPS5 system having highest conductivity (Fig. 8b).

This indicates the occurrence of faster ion dynamics after the addition of nanofiller as compared to polymer salt matrix (nanofiller free). It is important to note that this is in perfect correlation with the relaxation time obtained from complex permittivity analysis and conductivity value. The solid line in Fig. 8a, c is the fitted plot and is in perfect agreement with the experimental in the whole frequency window. Further, the effect of temperature is also examined on the loss tangent and relaxation time (Fig. 8c, d). Figure 8c shows that the relaxation peak shifts toward the high frequency with an increase of temperature and provides strong evidence of enhancement of ion migration. Also, the relaxation time displaying decreases with the increase in temperature [51]. It suggests that the thermal activation of charge carriers is a vital reason for the decrease of relaxation time and promotes faster ion migration.

### 3.9 Complex conductivity analysis

The complex conductivity is given as,  $\sigma(\omega) = \sigma' + i\sigma''$ . Here,  $\sigma'$  ( $= \omega\epsilon_o\epsilon''$ ) is the real part of complex conductivity,  $\sigma''$  ( $= \omega\epsilon_o\epsilon'$ ) is the imaginary part of complex conductivity,  $\epsilon_o$  is known as permittivity of free space, and  $\omega$  is the frequency. The frequency-dependent real part of complex permittivity is shown in Fig. 9a. The plot is divided in three regions depending on frequency. The low-frequency region is associated with electrode polarization and is followed by a frequency-independent dc conductivity region. Then with the increase of frequency increase in conductivity is attributed to the dispersion region. The low-frequency region shows an increase of the EP region, while at high-frequency dispersion region disappears with nanofiller content [74, 75]. The dc conductivity is extracted from the intercept corresponding frequency-independent region. The constant region in the intermediate frequency window is associated with the long-range ion migration from one coordinating site to another. It may be noted that the dc conductivity increases with nanofiller content and is maximum for the sample PPS5. This is in correlation with the impedance results [71, 76, 77]. Figure 9b shows the temperature-dependent real part of the complex conductivity for PPS5. The plot shows all three regions. With the increase of temperature, an increase in the electrode polarization region is due to the availability of more free charge carriers that build up polarization. This indicates the increase in conductivity and is observed from Fig. 9b. The increase of dc conductivity is evidenced by an increase in temperature. This confirms the thermally activated ion dynamics. Both Fig. 9a, b show the perfect fit with the experimental plot (shown by a solid line).

Figure 9c shows the frequency-dependent imaginary part of the complex conductivity for different nanofiller contents.

Initially, when we move from the high-frequency to low-frequency region, the decrease in conductivity is observed and minima is observed for a particular frequency, i.e., onset frequency ( $\omega_{on}$ ). This frequency indicates the start of electrode polarization buildup and conductivity increase is noticed. With a decrease of frequency, maxima in the conductivity is observed and it corresponds to the maximum frequency ( $\omega_{max}$ ). At this frequency, the buildup of electrode polarization is halted. With further, decrease of frequency, a decrease of conductivity is noticed for all plot. The PNC film with 5 wt% nanofiller (PPS5) shows maximum  $\omega_{on}$  and  $\omega_{max}$  value which has been used to find out time (Fig. 9e). The lowest time indicates the faster ion dynamics for this sample and is also in correlation to the relaxation time obtained from loss tangent analysis. Figure 9d shows the temperature-dependent imaginary part for PPS5. It may be observed that both  $\omega_{on}$  and  $\omega_{max}$  shift toward high frequency and indicates the temperature-controlled ion migration [34, 51]. The fitted plot is also in absolute agreement with the experimental plot.

### 3.10 Correlation of number density ( $n$ ), mobility ( $\mu$ ), and diffusion coefficient ( $D$ )

For examining the ion transport in PNC films, ionic conductivity, mobility, number of charge carriers, and diffusion coefficient need to be checked. So, for the present PNC films, these parameters are evaluated and their correlation is presented. The mobility ( $\mu$ ) is the ease of the ions to pass through the media when the external field is applied, while diffusion coefficient ( $D$ ) is the ease with which the ions pass in the presence of concentration gradient [78, 79]. Also, for strengthening the analysis, three different methods have been used to calculate the transport parameters ( $n$ ,  $\mu$ ,  $D$ ). The detailed equation is summarized in Table 3. The qualitative idea about all the three parameters is given as Eq. 2 and shows the direct relation of these parameters with the free ions. Figure 10 displays the variation of  $n$ ,  $\mu$ ,  $D$  via three different methods for varied nanofiller content. It may be noted that all parameters show an increasing trend with the addition of nanofiller in the polymer salt matrix. Figure 10b, c shows the maxima in  $\mu$ ,  $D$  for the 5 wt. % nanofiller content (PPS5). It needs to be mentioned here that the maxima in conductivity are also observed for this system. This is also in absolute correlation with the dielectric study, which shows the highest dielectric constant and lowest relaxation time for this system. The detailed values of parameters are summarized in Table 4.

### 3.11 Electrochemical performance study of electric double-layer capacitor cells

Figure 11b shows the schematic of the symmetric SC cell assembly used for the impedance, cyclic voltammetry, and

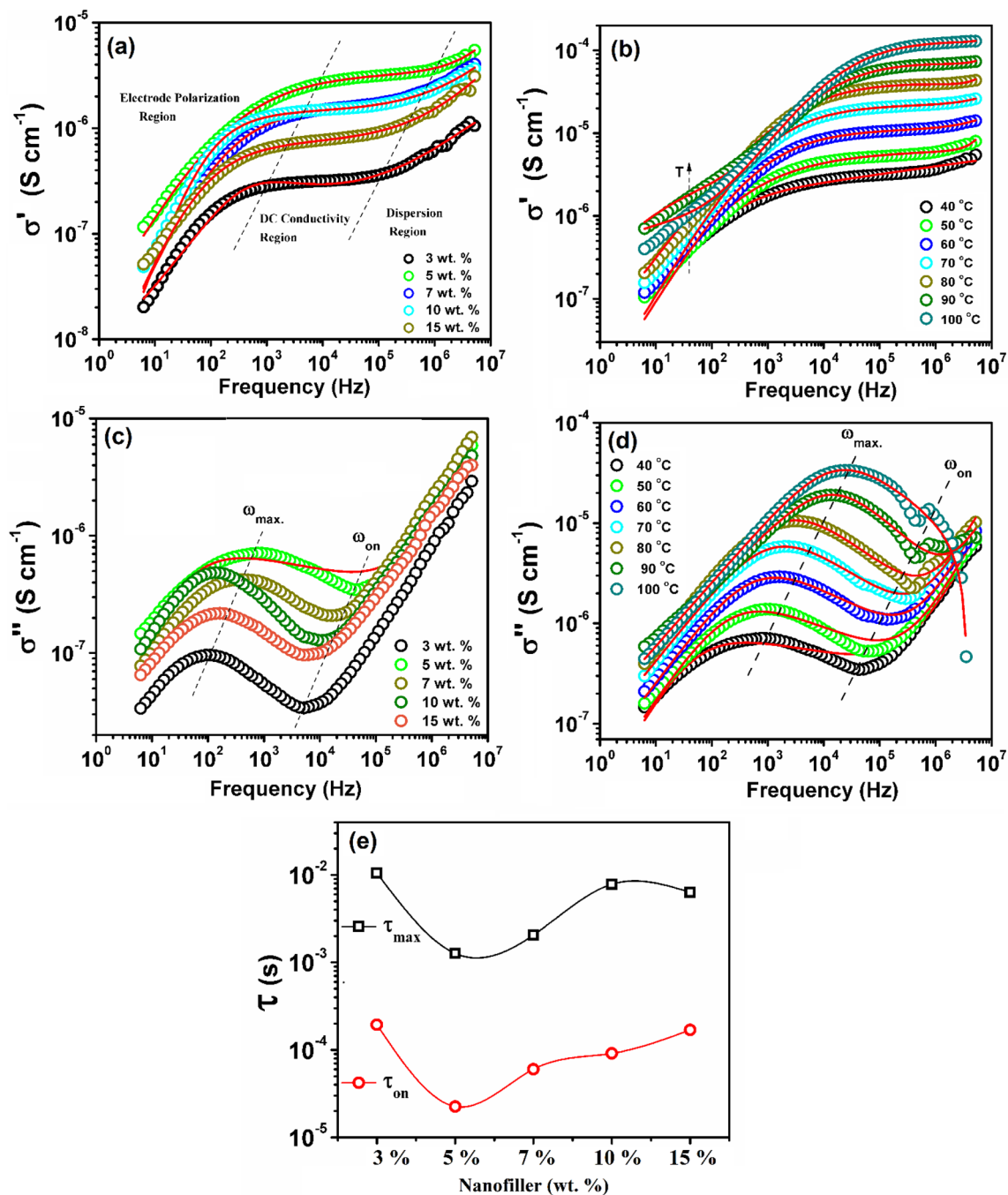


**Fig. 9** Frequency-dependent **a** real part, **b** temperature-dependent real part for PPS5, **c** imaginary part, **d** temperature-dependent imaginary part for PPS5, **e** variation of relaxation time for PNC films

charge–discharge measurement. The active material was carbon black/10%  $TiO_2$  composite and Ni foam is used as a current collector. The CV has been performed at different scan rates between 10 and 100 mV/s in the voltage window of  $-0.6$  to  $+0.6$  V. The CV curve signature indicates the non-ideal capacitive nature owing to the capacitive storage mechanism at the electrode/electrolyte interface. The

absence of the redox peaks in the CV reveals the absence of any Faradic reactions. With the increase of scan rate, the shape of the CV curve remains almost identical and enhancement in the area is observed. From the CV curve, the specific capacitance has been evaluated. The cell-specific capacitance ( $C_{sp}$ ) has been obtained using the following relation:



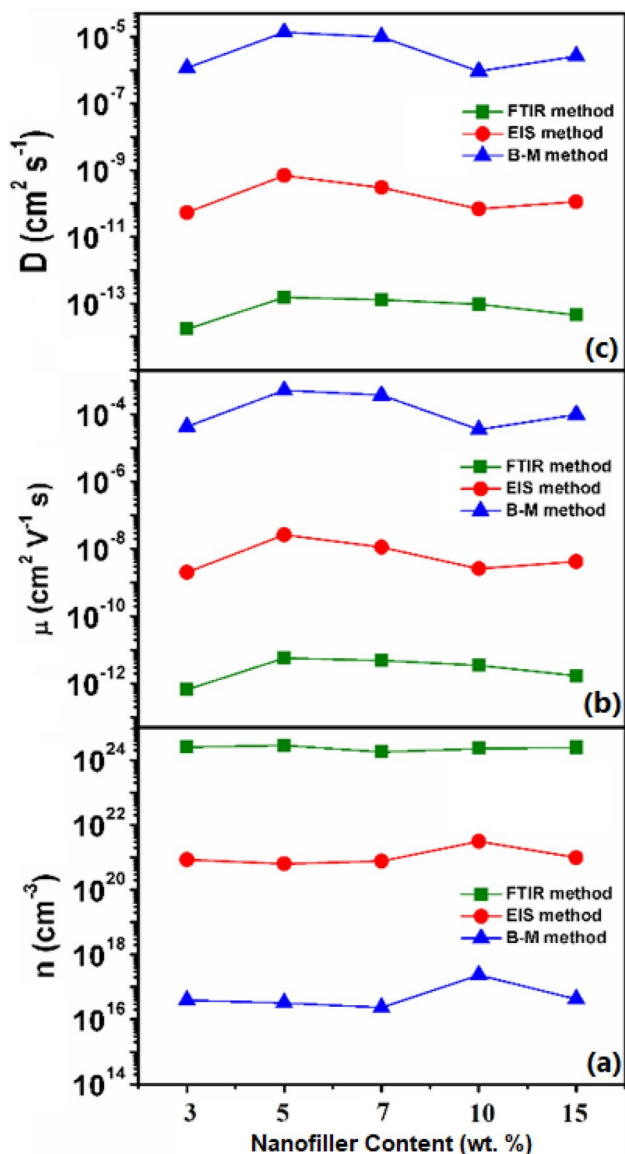


Fig. 10 Variation of **a** number density of charge carriers,  $n$ ; **b** ion mobility,  $\mu$ ; and **c** diffusion coefficient,  $D$

$$C_{\text{spec}} = \frac{1}{2 \times m \times v \times \Delta V} \int iV \partial V, \tag{4}$$

where  $V$  is the scan rate,  $\Delta V$  is the voltage range of CV curve, and  $m$  is the active material mass per electrode [80].

The variation of the specific capacitance at different scan rates is shown in Fig. 11d. The specific capacitance for the cell Ni foam/PNC/Ni foam is 134.16 F/g at 10 mV/s (Table 5). It may be noted that the specific capacitance decreases with the increase of the scan rate. At a low scan rate, all charge carriers get accommodated in the active material, while a high scan rate the whole electrode area is not used for storage, which is reflected in the decrease-specific capacitance. The high specific capacitance value of

the SC cell confirms the suitability of the prepared PNC film as the electrolyte. The PNC film provides sufficient ion migration and ions get accumulated on the electrodes that result in EDL formation.

The charge–discharge curve of the EDLC cell for different constant current densities is shown in Fig. 11c. The linear nature of the GCD curve is evidence of the non-Faradic charge storage mechanism. The linear nature also confirms the absence of any pseudo-capacitive nature associated with ion adsorption/desorption. This is also supported by the CV analysis, which indicates a non-Faradic charge storage mechanism. The overall specific capacitance has been evaluated using the formula as given below,

$$C_{\text{cell}} = \frac{i \times \Delta t}{m \times \Delta V}, \tag{5}$$

where  $i$  is the discharge current,  $\Delta t$  is the time taken for one discharge,  $m$  is the active mass of two electrodes, and  $\Delta V$  is the voltage of GCD. The plot of specific capacitance at different current densities is shown in Fig. 11e. It may be noted that the specific capacitance decreases with the increase of current density. The highest specific capacitance is 135.16 F/g at 0.02 A/g (Table 5). Further to support the EDLC cell performance, the specific energy density ( $E$ ) and specific power density ( $P$ ) are obtained. The values of  $E$  and  $P$  are evaluated using the following equations,

$$E = \frac{C_{\text{cell}} \times (\Delta V)^2}{7.2} \text{ (Wh/kg)} \tag{6}$$

$$P = \frac{E \times 3600}{\Delta t} \text{ (kW/kg)}, \tag{7}$$

where  $C_{\text{cell}}$  is the specific capacitance,  $\Delta t$  is the discharge time, and  $\Delta V$  is the working voltage range. The specific energy density and specific power density for the EDLC cell are 5.99 Wh/kg and 27.03 kW/Kg, respectively (at 0.02 A/g).

### 4 Conclusion

In the present work, we have demonstrated the effect of BaTiO<sub>3</sub> nanofiller on the structural, morphological, electrical, thermal, dielectric, and ion transport properties of PEO-NaPF<sub>6</sub> solid polymer electrolyte. The addition of nanoparticle suppresses the crystalline nature of polymer host (evidenced from XRD) and transition from crystalline to amorphous morphology is evidenced by FESEM. The FTIR spectrum indicates the polymer–ion, ion, and polymer–ion–nanofiller interaction and confirms the polymer nanocomposite formation. The electrical conductivity is enhanced with nanofiller addition and

**Table 3** Approaches to obtaining the number density ( $n$ ), mobility ( $\mu$ ) and diffusion coefficient ( $D$ )

Method	Bandara and Mellander (B–M) method	Impedance spectroscopy method	FTIR method
Units			
$D$ ( $\text{cm}^2\text{s}^{-1}$ )	$D = \frac{d^2}{\tau_2 \delta^2}$	$D = \frac{(k_2 \epsilon_r \epsilon_0 A d)^2}{\tau_2}$	$D = \frac{\mu k_B T}{e}$
$\mu$ ( $\text{cm}^2 \text{V}^{-1} \text{s}^{-1}$ )	$\mu = \frac{e d^2}{k T \tau_2 \delta^2}$	$\mu = \frac{e (k_2 \epsilon_r \epsilon_0 A d)^2}{k_B T \tau_2}$	$\mu = \frac{\sigma}{n e}$
$N$ ( $\text{cm}^{-3}$ )	$n = \frac{\sigma k T \tau_2 \delta^2}{e^2 d^2}$	$n = \frac{\sigma k_B T \tau_2}{(e k_2 \epsilon_r \epsilon_0 A d)^2}$	$n = \frac{M \times N_A}{V_{\text{Total}}} \times \text{freeionarea}(\%)$
Parameters	$\tau_2$ is a time constant corresponding to the maximum dissipative loss curve, $\delta = d/\lambda$ , $\lambda$ is the thickness of the electrical double layer, $d$ is half-thickness of the polymer electrolyte	$k_2$ and $k_1$ are obtained from the trial and error on the Nyquist plot, The value of $\tau_2$ was taken at the frequency corresponding to a minimum in the imaginary parts of the impedance, $Z_i$ , i.e., at $Z_i 0$ , $k_B$ is the Boltzmann constant ( $1.38 \times 10^{-23} \text{ J K}^{-1}$ ) and $T$ is the absolute temperature	$M$ is the number of moles of salt used in each electrolyte, $N_A$ is Avogadro's number ( $6.02 \times 10^{23} \text{ mol}^{-1}$ ), $V_{\text{Total}}$ is the total volume of the solid polymer electrolyte, and $\sigma$ is dc conductivity $e$ is the electric charge ( $1.602 \times 10^{-19} \text{ C}$ ), $k_B$ is the Boltzmann constant ( $1.38 \times 10^{-23} \text{ J K}^{-1}$ ) $T$ is the absolute temperature

**Table 4** The summary of number density ( $n$ ), mobility ( $\mu$ ), and diffusion coefficient ( $D$ ) by three approaches

EIS method						
Wt% nanofiller	$K_2$ ( $\times 10^3 \text{ F}^{-1}$ )	$\epsilon_r$ (at 100 kHz)	$\tau_2$ ( $\times 10^{-4} \text{ s}$ )	$n$ ( $\times 10^{18} \text{ cm}^{-3}$ )	$\mu$ ( $\times 10^{-6} \text{ cm}^2 \text{ V}^{-1} \text{ s}$ )	$D$ ( $\times 10^{-8} \text{ cm}^2 \text{ s}^{-1}$ )
3	4.14	1731	1.46	36.5	41.1	1.11
5	3.53	1618	1.45	67.7	26.1	70.4
7	6.36	1342	2.60	29.8	32.8	88.6
10	6.25	1610	1.77	14.9	66.7	1.80
15	19.8	1341	2.15	0.81	3.80	10.4
BM method						
Wt% nanofiller	$2d$ ( $\times 10^{-2} \text{ cm}$ )	$\tau_2$ ( $\times 10^{-4} \text{ s}$ )	$\delta$	$n$ ( $\times 10^{17} \text{ cm}^{-3}$ )	$\mu$ ( $\times 10^{-5} \text{ cm}^2 \text{ V}^{-1} \text{ s}$ )	$D$ ( $\times 10^{-7} \text{ cm}^2 \text{ s}^{-1}$ )
3	0.01	1.21	9.752	2.85	5.28	0.14
5	0.01	1.46	15.94	28.9	0.61	1.64
7	0.01	1.77	20.42	52.4	0.18	0.50
10	0.01	1.77	8.45	1.56	6.38	17.2
15	0.01	2.14	3.09	15.4	2.95	7.9
FTIR method						
Wt% nanofiller	$V_{\text{Total}}$ ( $\text{cm}^3$ )	FIA (%)	$\sigma$ ( $\times 10^{-6} \text{ S cm}^{-1}$ )	$n$ ( $\times 10^{24} \text{ cm}^{-3}$ )	$\mu$ ( $\times 10^{-12} \text{ cm}^2 \text{ V}^{-1} \text{ s}$ )	$D$ ( $\times 10^{-13} \text{ cm}^2 \text{ s}^{-1}$ )
3	0.02	45.12	2.41	2.51	0.66	0.17
5	0.02	52.29	2.83	2.88	5.66	1.52
7	0.02	47.10	1.57	1.79	4.85	1.31
10	0.02	51.68	1.60	2.26	3.52	0.95
15	0.02	44.09	0.50	2.45	1.68	0.45

temperature-dependent conductivity follows the Arrhenius nature. The optimum PNC film exhibits the highest conductivity and lowest activation energy. The almost unity value of the ion transference number confirms ionic conduction and a high electrochemical stability window ( $\sim 5 \text{ V}$ ) is observed

for the optimum system (PPS5). The high value of dielectric constant for the optimum system is due to more number of free charge carriers as evidenced from ion–ion interaction. The PNC films having the highest conductivity have low relaxation time as evidenced by the loss tangent and ac

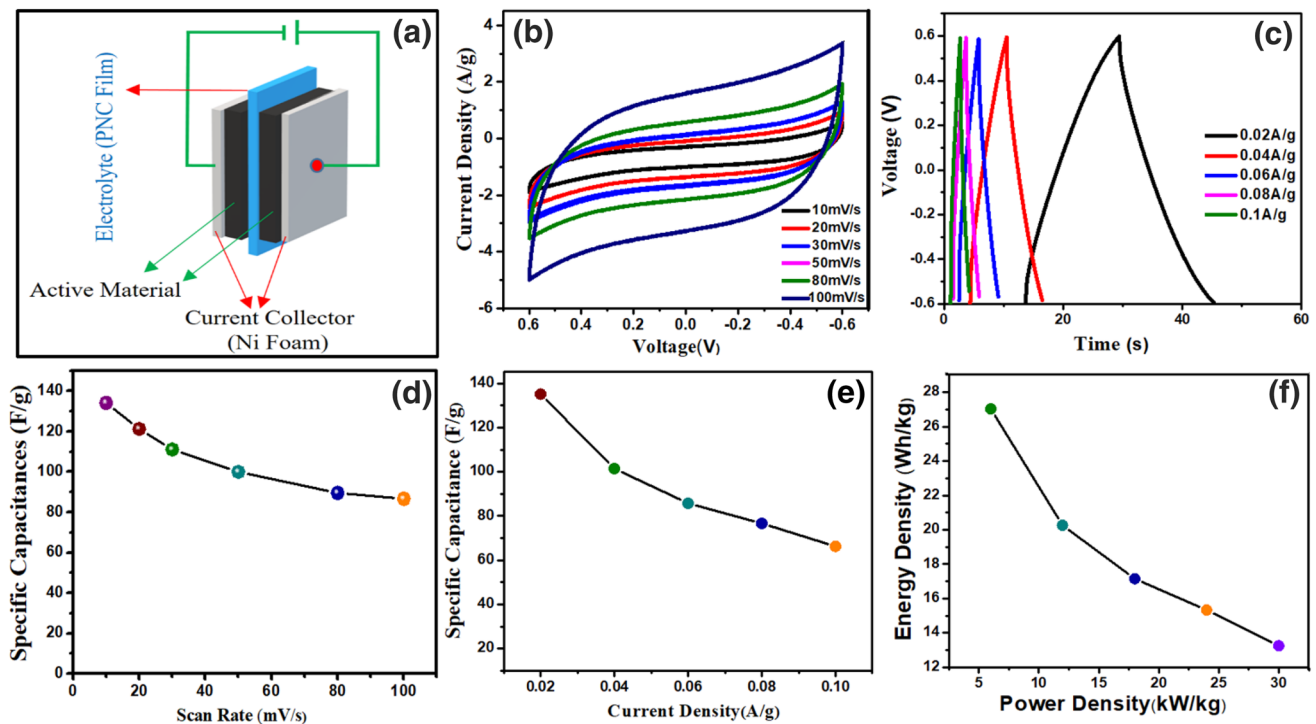


**Fig. 11** **a** Schematic of SC cell assembly, **b** cyclic voltammetry curves at various scan rates, **c** charge–discharge curves at different current densities, **d** variation of the specific capacitance of with scan

rates, **e** variation of the specific capacitance at different constant current densities, and **f** Ragone plot of energy and power density

**Table 5** Specific capacitance obtained from CV and GCD

CV		GCD			
s (mV/s)	$C_{\text{spec}}$ (F/g)	$I$ (A/g)	$C_{\text{spec}}$ (F/g)	$P$ (kW/kg)	$E$ (Wh/kg)
10	134.16	0.02	135.16	5.99	27.03
20	121.25	0.04	101.48	11.97	20.26
30	111.11	0.06	85.75	18	17.15
50	100.10	0.08	76.66	23.99	15.33
80	89.58	0.1	66.25	30	13.25

conductivity analysis. The temperature also enhances the ion dynamics as observed from an increase in dc conductivity, dielectric constant, and lowering of relaxation time. The ion transport parameters ( $n$ ,  $\mu$ ,  $D$ ) have been obtained by the FTIR, Complex Impedance spectroscopy, and Loss tangent method. All parameters show a perfect correlation with the conductivity and dielectric constant. The improved electrical and dielectric properties encouraged us to fabricate the EDLC cell using optimum PNC film as electrolyte and Carbon as an electrode. The prepared Electric double-layer capacitors (EDLC) show desirable performance. The specific capacitance of the EDLC cell is 134.16 F/g (10 mV/s). The specific energy density and specific power density for the EDLC cell are 5.99 Wh/Kg, and 27.03 kW/kg, respectively (at 0.02 A/g). In conclusion, the prepared polymer

nanocomposite has the potential to act as an electrolyte cum separator for supercapacitor applications.

**Author contributions** Both Mohit Madaan, and Ankit Kumar contributed equally in the sample preparation, characterization, and manuscript preparation. Both may be considered as first authors.

## References

1. A. Arya, A.L. Sharma, *Ionics* **23**, 497 (2017)
2. M. Winter, R.J. Brodd, *Chem. Rev.* **104**, 4245 (2004)
3. N.G. Saykar, R.K. Pilania, I. Banerjee, S.K. Mahapatra, *J. Phys. D. Appl. Phys.* **51**, 475501 (2018)
4. A. Arya, A.L. Sharma, *J. Mater. Sci.* **55**, 6242 (2020)
5. K. Mensah-Darkwa, C. Zequine, P.K. Kahol, R.K. Gupta, *Sustainability* **11**, 414 (2019)
6. J. Mindemark, M.J. Lacey, T. Bowden, D. Brandell, *Prog. Polym. Sci.* **81**, 114 (2018)
7. A. Arya, A.L. Sharma, *J. Solid State Electrochem.* **22**, 2725 (2018)
8. O.V. Yarmolenko, A.V. Yudina, K.G. Khatmullina, *Russ. J. Electrochem.* **54**, 325 (2018)
9. L. Yue, J. Ma, J. Zhang, J. Zhao, S. Dong, Z. Liu, G. Cui, L. Chen, *Energy Storage Mater.* **5**, 139 (2016)
10. A. Arya, M. Sadiq, A.L. Sharma, *Ionics* **24**, 2295 (2018)
11. A. Goren, C.M. Costa, M.T. Machiavello, D. Cintora-Juarez, J. Nunes-Pereira, J.L. Tirado, M.M. Silva, J.G. Ribelles, S. Lanceros-Mendez, *Solid State Ionics* **280**, 1 (2015)

12. M. Sadiq, A. Arya, A.L. Sharma, *Integr. Res. Adv.* **3**, 16 (2016)
13. B. Scrosati (ed.), *Applications of Electroactive Polymers*, vol. 75 (Chapman & Hall, London, 1993)
14. N. Srivastava, M. Kumar, *J. Solid State Electrochem.* **20**, 1421 (2016)
15. S. Ramesh, C.W. Liew, *Ionics* **16**, 255 (2010)
16. S. Ramesh, C.W. Liew, E. Morris, R. Durairaj, *Thermochim. Acta* **511**, 140 (2010)
17. C.W. Liew, R. Durairaj, S. Ramesh, *PLoS ONE* **9**, 0102815 (2014)
18. S.R. Raghavan, M.W. Riley, P.S. Fedkiw, S.A. Khan, *Chem. Mater.* **10**, 244 (1998)
19. S. Ramesh, T. Winie, A.K. Arof, *Eur. Polym. J.* **43**, 1963 (2007)
20. A. Jagadeesan, M. Sasikumar, R. Jeevani, H.A. Therese, N. Ananth, P. Sivakumar, *J. Mater. Sci. Mater. Electron.* **30**, 17181 (2019)
21. M. Hema, S. Selvasekerapandian, A. Sakunthala, D. Arunkumar, H. Nithya, *Phys. B Condens. Matter* **403**, 2740 (2008)
22. F. Yuan, H.Z. Chen, H.Y. Yang, H.Y. Li, M. Wang, *Mater. Chem. Phys.* **89**, 390 (2005)
23. M.M.E. Jacob, S.R.S. Prabaharan, S. Radhakrishna, *Solid State Ionics* **104**, 3 (1997)
24. J.H. Kim, M.S. Kang, Y.J. Kim, J. Won, N.G. Park, Y.S. Kang, *Chem. Commun.* **14**, 1662 (2004)
25. A. Arya, A.L. Sharma, *J. Phys. D Appl. Phys.* **50**, 443002 (2017)
26. P. Dhatarwal, R.J. Sengwa, *Polym. Bull.* **75**, 5645 (2018)
27. A. Arya, N.G. Saykar, A.L. Sharma, *J. Appl. Polym. Sci.* **136**, 47361 (2019)
28. J. Vondrák, J. Reiter, J. Velická, M. Sedlářiková, *Solid State Ionics* **170**, 79 (2004)
29. Pritam, A. Arya, A.L. Sharma, *Ionics* **1**, 22 (2019)
30. A. Arya, A.L. Sharma, *J. Solid State Electrochem.* **23**, 997 (2019)
31. Pritam, A. Arya, A.L. Sharma, *J. Mater. Sci.* **54**, 7131 (2019)
32. K.N. Kumar, M. Kang, K. Sivaiah, M. Ravi, Y.C. Ratnakaram, *Ionics* **22**, 815 (2016)
33. A. Arya, A.L. Sharma, *J. Phys. D Appl. Phys.* **51**, 045504 (2018)
34. A. Arya, A.L. Sharma, *J. Phys. Condens. Matter* **30**, 165402 (2018)
35. S. Choudhary, R.J. Sengwa, *Polym. Bull.* **72**, 2591 (2015)
36. A. Das, A.K. Thakur, K. Kumar, *Ionics* **19**, 1811 (2013)
37. S.A. Hashmi, H.M. Upadhyaya, A.K. Thakur, A.L. Verma, *Ionics* **6**, 248 (2000)
38. K.K. Kumar, M. Ravi, Y. Pavani, S. Bhavani, A.K. Sharma, V.V.R. Narasimha Rao, *J. Membr. Sci.* **454**, 200 (2014)
39. P. Prabakaran, R.P.P.S. Gurusamy, *J. Solid State Electrochem.* **21**, 1273 (2017)
40. C.M. Burba, R. Frech, *J Phys Chem B* **109**, 15161–15164 (2005)
41. A.K. Jonscher, *Dielectric Relaxation in Solids* (Chelsea Dielectric Press, London, 1983)
42. S.B. Aziz, M.G. Faraj, O.G. Abdullah, *Sci. Rep.* **8**, 14308 (2018)
43. Y. Zhao, C. Wu, G. Peng, X. Chen, X. Yao, Y. Bai, F. Wu, S. Chen, X. Xu, *J. Power Sources* **301**, 47 (2016)
44. S.R. Mohapatra, A.K. Thakur, R.N.P. Choudhary, *Ionics* **14**, 255 (2008)
45. Z. Li, G. Su, D. Gao, X. Wang, X. Li, *Electrochim. Acta* **49**, 4633 (2004)
46. A.L. Sharma, A.K. Thakur, *J. Appl. Polym. Sci.* **118**, 2743 (2010)
47. Y. Ato, M. Watanabe, K. Sanui, N. Ogata, *Solid State Ionics* **40**, 632 (1990)
48. A.L. Sharma, A.K. Thakur, *Ionics* **17**, 135 (2011)
49. A. Arya, M. Sadiq, A.L. Sharma, *Polym. Bull.* **76**, 5149 (2019)
50. L. Liu, L. Chu, B. Jiang, M. Li, *Solid State Ionics* **331**, 89 (2019)
51. A. Arya, A.L. Sharma, *Ionics* **25**, 1617 (2019)
52. T. Mohamed Ali, N. Padmanathan, S. Selladurai, *Ionics* **19**, 1115 (2013)
53. N. Vijaya, S. Selvasekarapandian, G. Hirankumar, S. Karthikeyan, H. Nithya, C.S. Ramya, M. Prabu, *Ionics* **18**, 91 (2012)
54. N.K. Karan, D.K. Pradhan, R. Thomas, B. Natesan, R.S. Katiyar, *Solid State Ionics* **179**, 689 (2008)
55. N. Tripathi, A.K. Thakur, A. Shukla, D.T. Marx, *Polym. Eng. Sci.* **58**, 220 (2018)
56. K. Kumar, M. Ravi, Y.M. Pavani, S. Bhavani, A.K. Sharma, V.V.R. Narasimha Rao, *J. Non-Cryst. Solids* **358**, 3205 (2012)
57. F.M. Reicha, M. El-Hiti, A.Z. El-Sonbati, M.A. Diab, *J. Phys. D. Appl. Phys.* **24**, 369 (1991)
58. P. Dhatarwal, R.J. Sengwa, S. Choudhary, *SN Appl. Sci.* **1**, 112 (2019)
59. R.J. Sengwa, P. Dhatarwal, *Electrochim. Acta* **338**, 135890 (2020)
60. V.R. Sunitha, S. Radhakrishnan, *Ionics* **22**, 2437 (2016)
61. P. Dhatarwal, R.J. Sengwa, *J. Polym. Res.* **26**, 196 (2019)
62. A.K. Jonscher, *J. Mater. Sci.* **13**, 553 (1978)
63. A. Arya, A.L. Sharma, *Polym. Bull.* **1**, 35 (2019)
64. R.J. Sengwa, S. Choudhary, P. Dhatarwal, *J. Mater. Sci. Mater. Electron.* **30**, 12275 (2019)
65. A. Roy, B. Dutta, S. Bhattacharya, *Ionics* **23**, 3389 (2017)
66. P. Dhatarwal, R.J. Sengwa, *Macromol. Res.* **1**, 15 (2019)
67. S. Ibrahim, S.M. Mohd Yasin, N.M. Nee, R. Ahmad, M.R. Johan, *Solid State Commun.* **1532**, 426 (2012)
68. A. Karmakar, A. Ghosh, *Curr. Appl. Phys.* **12**, 539 (2012)
69. A. Arya, A.L. Sharma, *Macromol. Res.* **27**, 334 (2019)
70. S. Chopra, S. Sharma, T.C. Goel, R.G. Mendiratta, *Solid State Commun.* **127**, 299 (2003)
71. A.L. Sharma, A.K. Thakur, *Ionics* **21**, 1561 (2015)
72. A. Arya, A.L. Sharma, *J. Mater. Sci. Mater. Electron.* **29**, 17903 (2018)
73. R.J. Sengwa, S. Choudhary, *J. Alloys Compd.* **701**, 652 (2017)
74. P. Dhatarwal, R.J. Sengwa, *Ionics* **26**, 2259 (2019)
75. A. Roy, B. Dutta, S. Bhattacharya, *RSC Adv.* **6**, 65434 (2016)
76. N. Shukla, A.K. Thakur, A. Shukla, D.T. Marx, *Int. J. Electrochem. Sci.* **9**, 7644 (2014)
77. S. Choudhary, R.J. Sengwa, *J. Appl. Polym. Sci.* **15**, 132 (2015)
78. A.K. Arof, S. Amirudin, S.Z. Yusof, I.M. Noor, *Phys. Chem. Chem. Phys.* **16**, 1856 (2014)
79. T.M.W.J. Bandara, M.A.K.L. Dissanayake, I. Albinsson, B.E. Mellander, *Solid State Ionics* **189**, 63 (2011)
80. S. Das, A. Ghosh, *J. Appl. Polym. Sci.* **137**, 48757 (2019)

**Publisher's Note** Springer Nature remains neutral with regard to jurisdictional claims in published maps and institutional affiliations.